A data-driven high spatial resolution model of biomass accumulation and crop yield Application to a fragmented desert-oasis agroecosystem

Chen, Qiting; Jia, Li; Menenti, Massimo; Hu, Guangcheng; Wang, Kun; Yi, Zhiwei; Zhou, Jie; Peng, Fei; Ma, Shaoxiu; More Authors

DOI
10.1016/j.ecolmodel.2022.110182

Publication date
2023

Document Version
Final published version

Published in
Ecological Modelling

Citation (APA)
Chen, Q., Jia, L., Menenti, M., Hu, G., Wang, K., Yi, Z., Zhou, J., Peng, F., Ma, S., & More Authors (2023). A data-driven high spatial resolution model of biomass accumulation and crop yield: Application to a fragmented desert-oasis agroecosystem. *Ecological Modelling*, *475*, Article 110182. https://doi.org/10.1016/j.ecolmodel.2022.110182

Ecological Modelling 475 (2023) 110182

Contents lists available at ScienceDirect

Ecological Modelling

journal homepage: www.elsevier.com/locate/ecolmodel

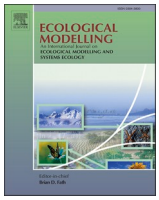

A data-driven high spatial resolution model of biomass accumulation and crop yield: Application to a fragmented desert-oasis agroecosystem

Qiting Chen [a], Li Jia [a,*], Massimo Menenti [a,b], Guangcheng Hu [a], Kun Wang [c], Zhiwei Yi [a], Jie Zhou [d], Fei Peng [e], Shaoxiu Ma [e], Quangang You [e], Xiaojie Chen [e], Xian Xue [e]

[a] State Key Laboratory of Remote Sensing Science, Aerospace Information Research Institute, Chinese Academy of Sciences, Beijing 100101, China
[b] Delft University of Technology, Delft, The Netherlands
[c] Key Laboratory of Digital Earth Science, Aerospace Information Research Institute, Chinese Academy of Sciences, Beijing 100094, China
[d] College of Urban and Environmental Science, Central China Normal University, Wuhan 430079, China
[e] Drylands Salinization Research Station, Key Laboratory of Desert and Desertification, Northwest Institute of Eco-Environment and Resources, Chinese Academy of Sciences, Lanzhou 730000, China

ARTICLE INFO

Keywords:
Crop yield estimation
Multi-source remote sensing data
High resolution
Heterogeneous agroecosystem

ABSTRACT

Information on crop yield is important for food security, in particular under the conditions of climate change and growing population worldwide. We developed a new fully distributed, high spatial resolution, model of biomass accumulation and crop yield applicable to a highly heterogeneous desert-oasis agroecosystem. The bulk of required input data is obtained by retrieving pixel-wise biogeophysical variables from a suite of very diverse satellite data. Both temperature and water stress conditions at field-scale are given full consideration, while the model was designed to strike a balance between model applicability and satisfactory characterization of the heterogeneous desert-oasis system to estimate field-scale yield. The development of this model relies on three main innovations. First, the start and end of the growing season were estimated for each pixel by calibrating the high spatial and temporal resolution observations of Normalized Difference Vegetation Index (NDVI) by Sentinal-2 (S2) MSI (Multi-Spectral Instrument) against limited local phenological information. Second, to monitor crop water stress, account taken of irrigation, a process-based water and energy balance model was applied to estimate the actual evapotranspiration (ET). This requires knowledge of soil water availability, which is characterized by downscaling the ASCAT (Advanced SCATterometer) soil moisture data product. To capture the dominant features of the eco-hydrological conditions in the desert and oasis agroecosystem, ET was further downscaled from the 1 km resolution. Third, likewise the water stress indicator, the air temperature stress indicator was mapped after characterizing the thermal contrast and heterogeneity of the desert-oasis system, by generating time series of air temperature at 1 km spatial resolution using the MODIS (Moderate Resolution Imaging Spectroradiometer) Land Surface Temperature (LST) data product. In the temporal dimension, gaps were mitigated by applying time series analysis techniques to reconstruct cloud-free time series of LST, NDVI, fAPAR and albedo. These innovations add up to a high resolution characterization of crop response to the geospatial variability of weather and climate forcing in the desert-oasis agroecosystem. The model was applied to the dominant crops, i.e., spring wheat, maize, sunflower, and melon, in the oases of the Shiyang River Basin (northwestern China) characterized by a rather fragmented land use. The high resolution of pixel-wise ecohydrological parameters, i.e., crop phenology, temperature stress and water stress factors successfully reflect differences of crops with different phenology and location in the oases. The relative errors for wheat and maize yields compared to the census data are less than 5% at district level. At the county level, the relative errors of wheat yields of Liangzhou, Minqin, Gulang, Jinchuan, and Yongchang equal to 0.87%, 24.2%, 9.7%, 12.5%, and 7.2%. For maize, the dominant crop, the error on estimated yields was less than 5%, except in Gulang. The relative error on estimated yield for sunflower was less than 10% compared to agricultural census data. The relative error on estimated melon yield was 16%. This performance highlights the applicability of the model to estimate field-scale yields in agroecosystems characterized by fragmented land use.

* Corresponding author.
E-mail address: jiali@aircas.ac.cn (L. Jia).

https://doi.org/10.1016/j.ecolmodel.2022.110182
Received 5 June 2022; Received in revised form 19 October 2022; Accepted 20 October 2022
Available online 3 November 2022

1. Introduction

The growing world population applies tremendous pressure on agriculture production and natural environmental resources, especially in developing regions. The global population is expected to reach 9.8 billions by 2050 (UNDESA, 2017). To meet the demands of population growth and the projected changes in dietary patterns in the future, global food production must increase by 70%−100% (Wart et al., 2013). Therefore, given such a dramatic requirement, both expansion of cultivated land and increased agricultural intensity will be needed, with further impact on the natural environment. The changing climate intensifies the risks of droughts and floods, which pose a significant threat to food production. Information on crop yield under limiting environmental conditions, such as due to water availability and quality, is therefore important for food security and environmental studies under the conditions of climate change and fast-growing population.

Modeling is a vital tool to obtain crop yield information at regional and global scales, especially because it allows to assess the expected performance of agroecosystems under changing climate and crop management conditions. The dynamic crop growth models, e.g., DSSAT (Decision-Support System for Agro-technology Transfer), WOFOST (WOrld FOod STudies), APSIM (Agricultural Production Systems sIMulator), and AquaCrop (FAO crop growth model) (Hijmans et al., 1994; Jones et al., 2003; Steduto et al., 2008; Holzworth et al., 2014), built upon crop biophysical processes, usually can achieve high accuracy in reproducing field-scale crop development and estimate yield, provided model parameters can be estimated accurately. To describe a specific crop or variety, these models require a detailed set of plant parameters to model e.g., phenology, assimilation, and partitioning of assimilates, which typically must be based on field trials on the crop or variety of interest. Applications at the regional/global scale, however, are hampered by the limited availability of a wide range of agronomic input data needed by such models and uncertainties are also associated with the parameterization of biogeochemical processes. Literature documents advances in blending satellite remote sensing data with dynamic crop growth models by e.g., data assimilation to improve the regional performance (de Wit and van Diepen, 2007; Jin et al., 2018; Huang et al., 2019; Liu et al., 2019). However, data assimilation is usually designed for only one or two state variables, e.g., soil moisture, leaf area index or Land Surface Temperature (LST), and uncertainty remains significant. In addition, when applied to regions with fragmented land uses and complex cropping patterns, a high spatial resolution model configuration is needed, which requires large computing resources.

Various satellite remote sensing observations can provide information reflecting the spatial and temporal features in the crop pattern and conditions, e.g., crop type, crop phenology and health condition. An alternative way is using a remote-sensing-data-driven model yet with a robust bio-physical basis. In these models, biomass accumulation is estimated by applying the Light Use Efficiency (LUE) concept, according to Monteith (1972), through the crop growing season, while parameterizations are applied to estimate crop yield from biomass. LUE is defined as the biomass produced by photosynthesis per unit of absorbed radiant energy. The LUE-based method combines the solar Photosynthetically Active Radiation (PAR), the intercepted fraction of PAR (fAPAR: the fraction of Absorbed Photosynthetically Active Radiation by vegetation) and the PAR utilization efficiency to determine the daily biomass accumulation. In theory, the LUE-based method is consistent with detailed biophysical models of photosynthesis under the reasonable hypothesis that multiple biochemical processes combine to determine optimal photosynthesis (Haxeltine and Prentice, 1996).

In practice, the actual PAR utilization efficiency in the LUE-based models is expressed as the product of an optimal LUE with a number of stress factors. The main difference in the LUE-based models is the definition and estimation of the parameters being used to down-regulate the optimal biomass accumulation rate to the actual rate, since the biogeochemical controls on LUE are still poorly understood. For example, the CASA (Carnegie-Ames-Stanford Approach) (Potter et al., 1993) takes into account the variation of LUE with seasons and biomes. Field et al. (1995) further improved the LUE-based modeling by considering limitations due to temperature and water deficit. The GLO-PEM2 (GLObal Production Efficiency Model) and MODIS-PsN (MODIS - Moderate Resolution Imaging Spectroradiometer, Daily Photosynthesis) adopted Vapor Pressure Deficit (VPD) to express the water stress (Goetz et al., 2000; Zhao et al., 2005). LUE-based models have been implemented as a core element of systems for large area monitoring of biomass and crop yield estimations taking advantage of remote sensing data (Gower et al., 1999; Veroustraete et al., 2002; Bastiaanssen and Ali, 2003; Zwart et al., 2010; Teixeira et al., 2013). Such systems are also being operated in an operational context, such as in the MARSOP (Monitoring Agriculture through Remote Sensing techniques) system (http://www.marsop.info) and in the Global Land component of the GMES (Global Monitoring for Environment and Security) Initial Operations (GIO-GL) (Van Hools and Eerens, 2015).

Notwithstanding these successful experiences, challenges still exist and were addressed in this study. In a highly heterogenous desert-oasis agroecosystem with fragmented land uses and complex crop patterns, crop conditions must be characterized as a spatial resolution adequate to capture both the heterogeneity within the oases and the contrast with the surrounding desert area. Hydrological conditions must be monitored at a spatial resolution consistent with such variability to understand the crop response to weather and climate forcing. Specifically, this applies to crop phenology and related biophysical variables, to soil water availability and to thermal conditions. On the other hand, in practice, the retrieval of information on hydrological conditions and surface temperature obtained from infrared and microwave observations is frequently hampered by low spatial resolution. Besides, optical and thermal remote sensing observations are often contaminated by weather conditions, with considerable impacts on the estimation of fAPAR, NDVI, albedo, and land surface temperature (LST). Time series reconstruction is therefore needed to obtain gap-free essential variables to estimate crop biomass accumulation at high temporal resolution.

The innovations we deployed to address these challenges add up to a high resolution model characterizing the crop response to the geospatial variability of weather and climate forcing in the desert-oasis agroecosystem. The development of this model relies on three main innovations. First, the start and end of the growing season were estimated for each pixel by calibrating the high spatial and temporal resolution observations of NDVI by Sentinal-2 (S2) MSI (Multi-Spectral Instrument) against limited local phenological information. The high temporal frequency of S2 / MSI makes it possible to retrieve directly the temporal evolution of relevant biophysical variables related to crop phenology without using an approximate method such as the application of temperature sums. Second, to monitor crop water stress, account taken of irrigation, we use a process-based water and energy balance model, ETMonitor (Hu and Jia, 2015; Cui and Jia, 2021; Zheng et al., 2022), to estimate the actual evapotranspiration (ET), which requires knowledge of soil water availability, monitored by using satellite observations of soil moisture. To mitigate the gap in spatial resolution with the field-scale information on crop conditions, soil moisture was estimated using the ASCAT (Advanced SCATterrometer) soil moisture data downscaled to MODIS LST resolution. The relationship between the downscaled soil moisture and the predictors, i.e., LST, NDVI, albedo, DEM (Digital Elevation Model), and location, was constructed using a machine learning model. To capture the dominant features of the eco-hydrological conditions in the desert and oasis agroecosystem, the ET was further downscaled from the 1 km resolution. Third, likewise the water stress indicator, the air temperature stress indicator was mapped after characterizing the thermal contrast and heterogeneity of the desert-oasis system, by generating time series of air temperature at 1 km spatial resolution using the MODIS LST data product. In the temporal dimension, gaps were mitigated by applying time series analysis techniques to reconstruct cloud-free time series of LST, NDVI, and albedo.

2. Study area and data

2.1. Study area

The Shiyang River Basin (SRB) is one of the three inner drainage river basins in Hexi Corridor, northwestern China, located between 101°41′E and 104°16′E, 36°26′N and 39°27′N (Fig. 1). It originates from the cold and semi-arid Qilian Mountains in the south and ends in the temperate and arid desert-oasis region in the north, occupying an area of 41,600 km^2. The SRB covers the main areas of Liangzhou, Minqin, Jinchang, Yongchang, and Gulang Counties. The river water supply primarily comes from rainfall and glacier and snow melting in the Qilian mountain area.

The oases in the SRB play a vital role in the water and food security of northwestern China. The growing season is April to October. The annual precipitation in the agricultural area varies from 100 to 300 mm, while the potential ET is 1200 to 2000 mm (Wang et al., 2012). Thus, local agriculture heavily relies on irrigation. To keep the pace with the local economic development, the water and land resources have been over-exploited mainly for agriculture, which induced a severe ecosystem crisis. Water conflicts arose between ecosystem preservation and agriculture and between different sub-regions (Li et al., 2007; Xue et al., 2015). The agricultural area of the SRB is characterized by fragmented land use and complex cropping pattern (Xue et al., 2015). The dominant food crops are spring wheat and maize, and local high-value crops are sunflower and melon. Crop yield and ET estimates can provide

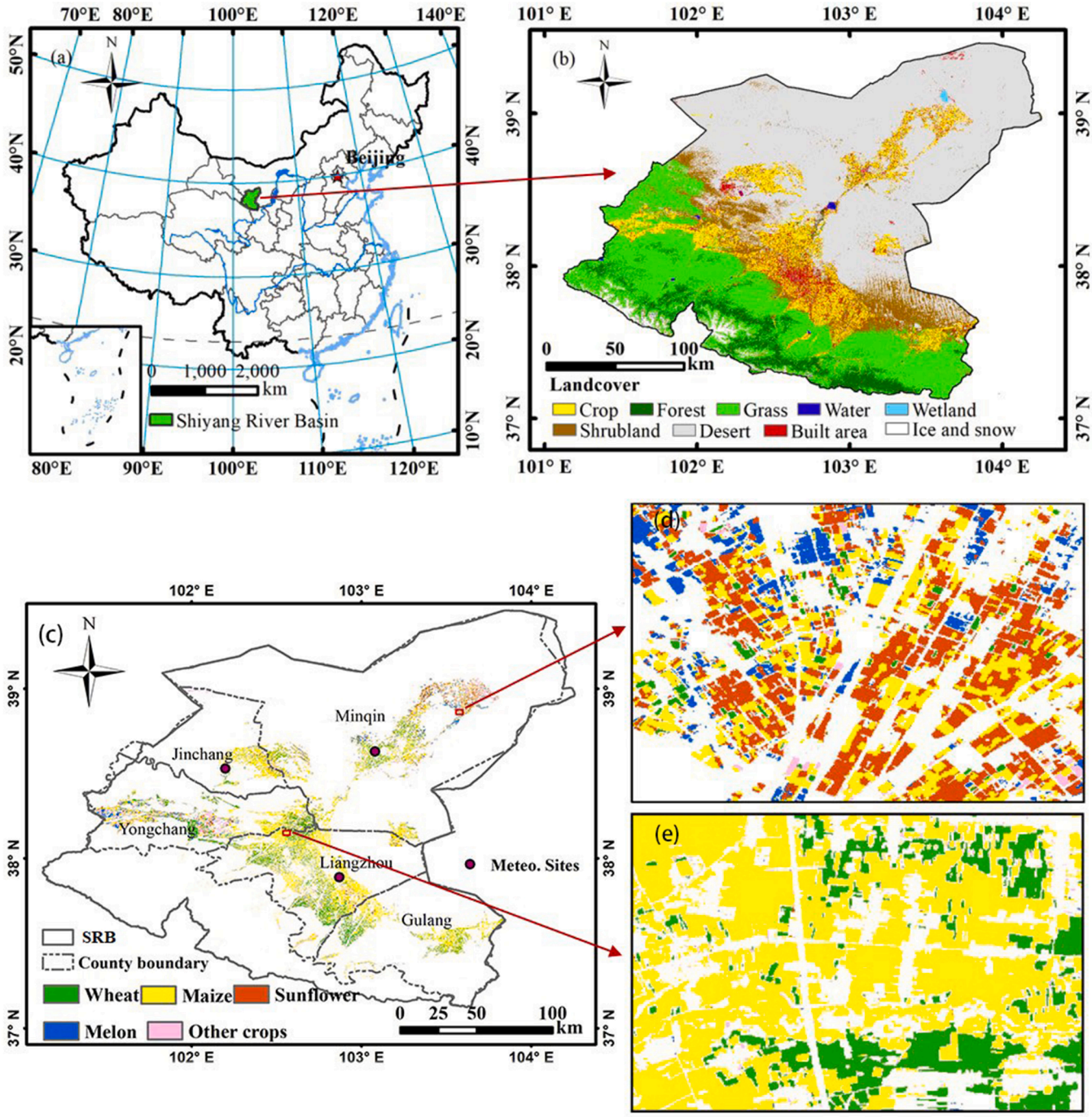

Fig. 1. Location map of the SRB (a), landcover (b) and crop classification (c); examples of full 10 m resolution crop maps (d) and (e).

meaningful spatial and temporal information for a comprehensive understanding of the water productivity of the region and support effective decision-making.

2.2. Remote sensing data

The remote sensing data applied in this study (Table 1) include the S2 / MSI surface reflectance (SR) data products, MODIS land surface products of LST, NDVI, and albedo, ASCAT surface soil moisture saturation products, SRTM (Shuttle Radar Topography Mission) DEM, and a predefined crop classification map.

The S2 mission was launched in 2015 by ESA (European Space Agency) to service wide-swath, high spatial and temporal resolution, and multi-spectral land monitoring. The MSI can provide observations with 10 m spatial resolution in four spectral bands, i.e., the three classical RGB bands and a Near Infra-Red (NIR) band. The S2 system is designed for global crop growth monitoring with a 5-day revisiting interval. In this study, we specifically adopted the S2 / MSI level-2 Bottom Of Atmosphere (BOA) reflectance data product (https://scihub.copernicus.eu/) in Band 4 (Red band, with central wavelength ~665 nm) and Band 8 (Near Infrared band, with central wavelength ~833 nm) to estimate NDVI and fAPAR during the growing season of 2019 in the study area.

The MODIS land surface products (http://lpdaac.usgs.gov/), including MOD11A1 (Land Surface Temperature), MOD13A2 (NDVI), and MCD43A3 (albedo) in 2019 were selected for air temperature and ET estimation. The MCD43A3 data were resampled to 1 km by linear interpolation to match the other MODIS data products before further processing.

The daily ASCAT dataset (https://land.copernicus.eu/global/products/swi) of surface soil moisture saturation at 0.1° was also used as input to the ET estimation model, i.e., ETMonitor. When applying the ETMonitor model, the 0.1° ASCAT dataset was first downscaled and projected to the same spatial resolution of 1 km MODIS data (see Sect. 3.5).

A 10 m crop classification map for 2019 (Fig. 1) was generated by applying a machine learning method to the multi-spectral and multi-temporal S2 / MSI surface reflectance data. The validation based on ground observations shows that the overall classification accuracy is 90% (Yi et al., 2020).

2.3. Reanalysis meteorological data

The gridded daily meteorological data required to estimate ET and Absorbed Photosynthetically Active Radiation (APAR) conditions, i.e., surface pressure, wind speed, relative humidity, precipitation, downward shortwave radiation, and downward longwave radiation, were extracted from the ERA5 reanalysis dataset (http://apps.ecmwf.int/datasets/) of ECMWF (European Centre for Medium-Range Weather Forecasts). The ERA5 dataset has an original spatial resolution of 0.25° and was downscaled to 1 km using SRTM DEM (Stahl et al., 2006; Gao and Giorgi, 2008; Hu and Jia, 2015).

Table 1
Remote sensing dataset used in this study.

Variables	Products	Temporal resolution	Spatial resolution
BOA reflectance at Band 4&8	Sentinel-2	5 days	10 m
LST	MOD11A1	Daily	1 km
NDVI	MOD13A2	16 days	1 km
Albedo	MCD43A3	Daily	500 m
Soil Moisture	ASCAT	Daily	0.1 °
DEM	SRTM	–	30 m
Crop types	Crop map	Yearly	10 m

2.4. Ground measurements

To estimate the temperature stress factors regulating the biomass accumulation, we used the daily mean air temperature measured at three meteorological ground stations (Table 2) in the oasis. The data collected in the period from March to November 2019, covering the main growing season of Shiyang river basin, were applied to parameterize the relationship between LST and the mean daily air temperature. The locations of ground sites are shown in Fig. 1c.

2.5. Agricultural census data

The agricultural census data on crop yield is officially reported in the Gansu Development Yearbook 2020 (Gansu Development Yearbook Editorial Committee, 2021).

3. Methods

Model overview. In the proposed model to estimate crop biomass accumulation, both temperature and water limitations were given full consideration to adjust the optimal crop growth rate to the actual rate. The timely and spatially detailed biophysical information needed to model biomass accumulation and yield formation, i.e., crop type, phenological development, APAR, air temperature stress, and water stress was retrieved by addressing the challenges identified in the Introduction. To this end, a remote sensing data driven framework to ingest S2 / MSI at-surface spectral reflectance, MODIS land surface products, ASCAT surface soil moisture saturation data, SRTM DEM, and ERA5 reanalysis meteorological data was developed. Remote sensing multi-spectral information was combined to capture the pixel-wise real crop growth status related to crop-specific properties, environmental constraints, and the field management. The model was designed to strike a balance between model applicability and satisfactory characterization of the heterogeneous desert-oasis system to estimate field-scale yield.

The proposed model (see Fig. 2) to estimate biomass accumulation and crop yield at high spatial resolution includes the following elements: (1) Time series reconstruction of remote sensing data; (2) Crop phenology estimation; (3) APAR estimation; (4) Estimation of air temperature stress factor; (5) Downscaling of soil moisture; (6) Estimation of ET and Rn and water stress; (7.1) Estimation of biomass by LUE model and (7.2) crop yield.

The following paragraphs describe in detail the seven elements of the model.

3.1. Time series reconstruction of remote sensing observations

In the proposed method, the pixel-wise crop emergence and harvest dates and the fAPAR, were estimated using the time series of S2 / MSI NDVI, taking advantage of the high spatial and temporal resolution. The daily water stress condition was estimated from the daily ET, which requires time series of MODIS NDVI and albedo. The daily air temperature stress was estimated from 1 km LST using the method by Alfieri et al. (2013), in which time series of MODIS LST is required.

The NDVI, albedo, and LST derived from satellite observations are often contaminated by clouds, which hampers their application to observe terrestrial vegetation properties. To obtain a spatially and temporally continuous NDVI, albedo, and LST dataset, the method of Harmonic Analysis of Time Series (HANTS) was applied to the S2 / MSI

Table 2
Meteorological ground stations in the oasis area of the SRB.

Station	Latitude N (^{0})	Longitude E (^{0})	Altitude (m)
Minqin	38.63	103.08	1367.5
Wuwei	37.89	102.87	1540.2
Jinchang	38.53	102.20	1508.9

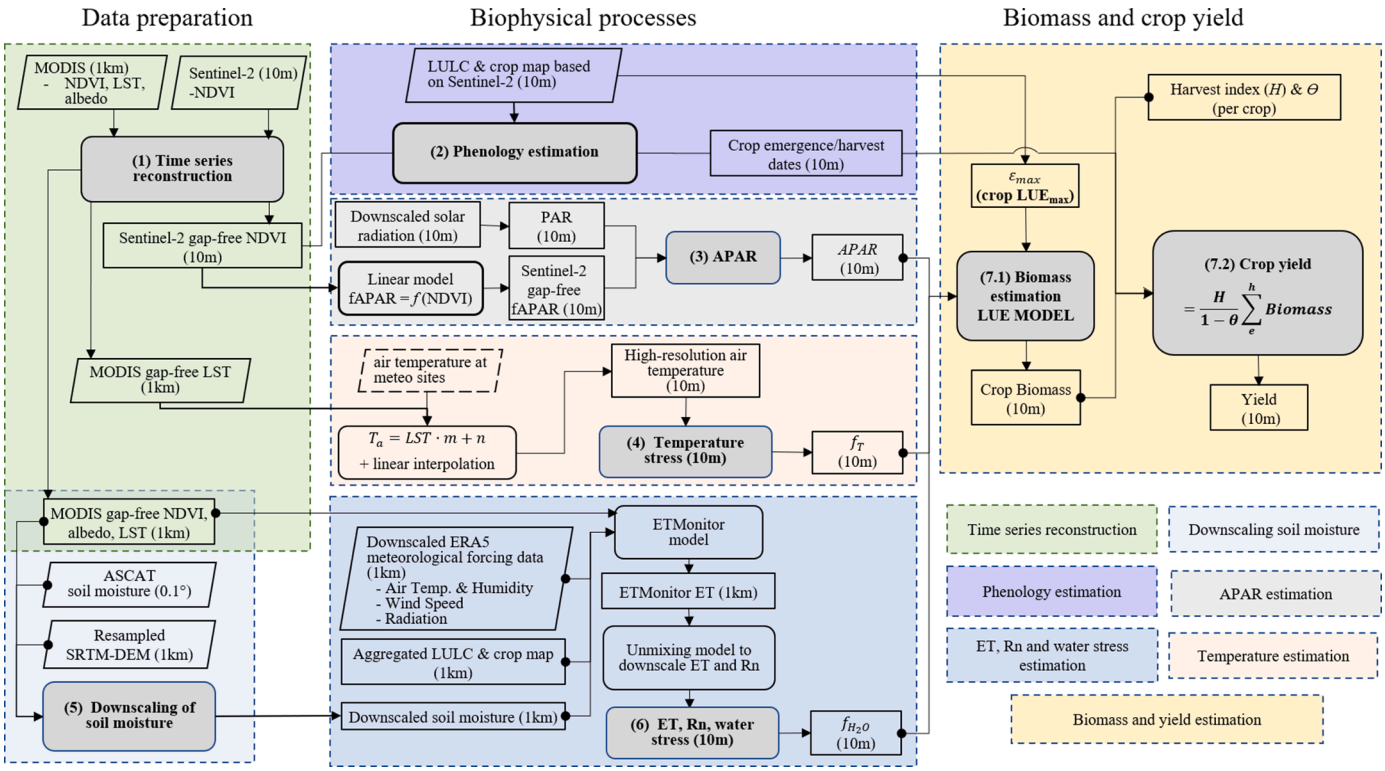

Fig. 2. Workflow of the high resolution modeling system to estimate biomass accumulation and crop yield.

NDVI and MODIS NDVI, albedo, and LST products to remove the cloud influence (Menenti et al., 1993; Verhoef, 1996; Roerink et al., 2000; Hadipour, 2021; Zhou et al., 2021).

The HANTS method decomposes a time series into several frequency components based on the concept of a discrete Fourier transform. Considering that albedo and NDVI change gradually driven by vegetation phenology, we applied four frequencies with periods equal to 360 days, 180 days, 120 days, and 90 days, respectively, in HANTS, to capture the seasonal variation of NDVI and albedo in the study area. Besides the four frequencies reflecting seasonal variability, to reconstruct the LST time series, we added two more frequencies with periods equal to 30 days and 15 days to capture the short-term variability due to possible fluctuations of atmospheric/weather conditions.

Cloud-contaminated observations are identified by HANTS as outliers and assigned a lower weight prior to a new iteration in the reconstruction of the time series. The analyst needs to specify whether outliers are positive or negative anomalies relative to the current reconstruction of the time series. Cloud-contaminated observations give negative values of NDVI and LST, so outliers in NDVI and LST time series are defined as negative anomalies. Given the high albedo of clouds, outliers in albedo are defined as positive anomalies and lower weights are given to the higher outliers, which is contrary to the situation of NDVI and LST. Zhou et al. (2016) evaluated the accuracy of HANTS in the reconstruction of noisy and cloud-contaminated observations in comparison with four other methods and documented the generally good performance of HANTS.

3.2. Crop phenology estimation

The crop emergence and harvest dates identify the period of time available for biomass accumulation during the growing season and then obtain the final yield. In the proposed model, the pixel-wise crop emergence and harvest dates, were estimated by applying crop-specific thresholds to the gap-free time series of S2 / MSI NDVI. This was made possible by the high spatial and temporal resolution. First, local knowledge indicated typical emergence and harvest dates applicable to the entire area (Table 3). Second, the NDVI values at these typical emergence and harvest dates were extracted for each crop from the spatially averaged NDVI temporal profiles - NDVI (t) (Fig. 3). Third, these NDVI values were applied as thresholds to the pixel-wise annual NDVI temporal profile to estimate the emergence and harvest dates for each crop and for each pixel. This method considers the specific characteristics of different crops and makes effective use of limited local phenological knowledge to determine the NDVI thresholds at the emergence and harvest dates in the growing season, valid for the entire study area. This solution was feasible because of the relative uniformity of local climate and of farming practices, i.e., leading to limited variability in the emergence and harvest dates.

3.3. APAR estimation

The photosynthetically active radiation absorbed by the vegetation APAR (MJ/m^2/day), defined as:

$$APAR = fAPAR \cdot PAR \quad (1)$$

where PAR (MJ/m^2/day) is the solar irradiance in the spectral range between 0.4μm and 0.7μm where the absorption bands of photosynthetic pigments are located. We followed the generally accepted approximation that on average daily PAR is 48% of the daily at-surface downward shortwave irradiance (between 0.4μm and 2.5μm) (McCree, 1972). The solar energy absorption by leaf pigments in the red band and high reflectance in the NIR band make the NDVI an appropriate

Table 3
The typical emergence and harvest dates applied to estimate the phenological NDVI thresholds for each crop in the study area.

Crop type	Wheat	Maize	Sunflower	Melon
Emergence	Apr. 5	May 15	May 20	Jun. 1
Harvest	Jul. 25	Oct. 1	Sept. 15	Sept. 20

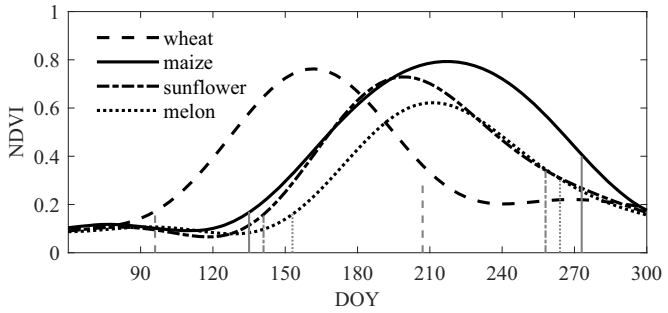

Fig. 3. Daily NDVI time series by HANTS for wheat, maize, sunflower, and melon in 2019 in the SRB; the vertical lines indicate the emergence and harvest dates based on local knowledge (Table 3); the NDVI values at these dates were applied to the pixel-wise NDVI(t) to estimate the pixel-wise emergence and harvest dates.

indicator to estimate fAPAR. A wealth of studies explored the relationship between fAPAR and NDVI (Daughtry et al., 1992; Myneni and Williams, 1994; Chen, 1996; Gitelson et al., 2014). We use the linear equation proposed in Bastiaanssen and Ali (2003) as applicable to multiple crops:

$$fAPAR = 1.257\mathrm{NDVI} - 0.161 \ (\text{with } fAPAR = 0 \ if \ fAPAR < 0) \tag{2}$$

3.4. Estimation of temperature stress factor

Air temperature (T_a) is an important parameter influencing the activity of key enzymes in photosynthesis, which is reflected by the temperature stress factor (f_T). The temperature stress factor includes two terms (f_{T_1} and f_{T_2}) here:

$$f_T = f_{T_1} \cdot f_{T_2} \tag{3}$$

$$f_{T_1} = 0.8 + 0.02T_{opt} - 0.0005{T_{opt}}^2 \tag{4}$$

$$f_{T_2} = \frac{1.1814}{1 + \exp\left(0.2\left(T_{opt} - 10 - T_{mon}\right)\right)} \cdot \frac{1}{1 + \exp\left(0.3\left(-T_{opt} - 10 + T_{mon}\right)\right)} \tag{5}$$

where T_{opt} (°C) denotes the temperature when photosynthetic efficiency reaches the maximum value and $T_{mon\ (°C)}$ is the monthly mean air temperature. f_{T_1} reduces crop growth rate in very cold and hot habitats, and f_{T_2} reflects a seasonal depression of crop growth rate when temperature departs from the optimal temperature. Field et al. (1995) proposed to estimate T_{opt} as the mean air temperature in the month when NDVI reaches the maximum value.

In a desert and oasis landscape, thermal heterogeneity of the land surface and the local variation of air temperature is not negligible. For regional-scale applications, the gridded T_a is usually obtained by interpolating data collected at meteorological ground stations or provided by reanalysis datasets (with grid resolution at 0.1 - 0.5°). Application of such data will smooth out the main thermal heterogeneity, given the sparseness of the stations and the coarse grid of reanalysis datasets, especially for small, fragmented regions like the SRB. In this study, the mean daily air temperature at 1 km resolution was applied to estimate biomass and yield at 10 m spatial resolution, assuming meteorological conditions over 1 km extent did not change dramatically. The 1 km daily mean air temperature T_a was estimated based on daily observations of LST (MOD11A1, 1 km) using the approach proposed by Alfieri et al. (2013). A linear relationship (Eq. (6)) between LST and the daily mean T_a measured at ground stations is established and further applied to obtain the gridded daily mean air temperature at the same resolution of the remotely sensed LST (i.e., 1 km, much higher than that of reanalysis datasets),

$$T_a = LST \cdot m + n \tag{6}$$

where m and n are coefficients. For areas within the same climate zone, m and n can be applied for an entire region.

In this study, the gap-free LST time series generated from the MODIS LST product and T_a observations from three meteorology stations in the oasis area for the whole year in 2019 were used to establish the relationship described in Eq. (6). Thus gap-free daily T_a at 1 km resolution were obtained for the entire SRB and aggregated to estimate the monthly temperature stress factors f_{T_1} and f_{T_2}. The 10 m f_{T_1} and f_{T_2} were obtained through linear interpolation to match the grid size of the other input data.

3.5. Downscaling of soil moisture

As regards the estimates of ET and the water stress indicator, one of the significant uncertainties is the low spatial resolution and discontinuous soil moisture data. At present, ASCAT soil moisture dataset is a long-term dataset with a relatively high spatial resolution (0.1 Degree) and is publicly available. Thus, in this study, a spatially continuous soil moisture dataset at high spatial resolution (1 km) was generated by downscaling the ASCAT soil moisture data utilizing multi-source remote sensing data and the Random Forest (RF) machine-learning model (Breiman, 2001).

The covariance matrix to apply RF machine-learning model includes LST, NDVI, albedo, DEM, longitude, and latitude. The spatial patterns of the soil moisture in this arid/semi-arid region are mainly driven by precipitation and agricultural activities, which are related to the geographical location, elevation, temperature, and vegetation characteristics. These facts provide a good physical basis to downscale the soil moisture by applying the RF machine-learning model with the selected covariates.

First, the 1 km, gap-filled MODIS LST, NDVI and albedo, DEM, longitude, and latitude were aggregated to the ASCAT grid scale. Then, the RF model was trained to obtain the relationship between the ASCAT soil moisture and the covariates. Finally, the trained RF machine-learning model was applied to the covariates at high spatial resolution (1 km) to obtain a spatially continuous soil moisture dataset with 1 km resolution.

3.6. Estimation of ET and Rn and the field-scale water stress factor

The indicator of water stress f_{H_2O} (dimensionless) is set equal to the Evaporative Fraction (EF) which better reflects the water availability to crops than vapor pressure deficit (VPD):

$$f_{H_2O} = EF = \lambda ET \ / \ (Rn - G) \tag{7}$$

where λET (W/m^2) is the bulk latent heat flux of the soil-vegetation unity, λ (J/kg) is the latent heat of ET (mm), Rn (W/m^2) is the total net radiation flux, and G (W/m^2) is the conductive heat flux from soil surface to deeper soil layer.

In this study, a water and energy balance model, ETMonitor (Hu and Jia, 2015; Cui and Jia, 2021; Zheng et al., 2022), was used to estimate the daily ET. The inputs of ETMonitor include key surface properties, i.e., soil moisture, NDVI, albedo, and land cover, and atmospheric variables, i.e., air temperature, wind speed, air humidity, pressure, precipitation and at-surface downward shortwave and longwave radiations. The model equations and detailed description can be found in Hu and Jia (2015) and Cui and Jia (2021).

Retrievals of actual ET by ETMonitor based on remote sensing data can capture the effects of irrigation, thus reflecting the actual irrigation water depths to some extent when lacking ancillary in-situ data. The performance of ETMonitor to derive actual ET over nearby irrigated oases of the Heihe river basin, which has a similar climate and land cover, had been evaluated based on the eddy covariance data (Hu and

Jia, 2015). The results show that ETMonitor provides satisfactory ET estimates with R^2 (the square of the correlation coefficient) and RMSE (the root mean square error) equal to 0.92 and 0.59 mm/day, respectively.

The pixel-wise daily R_n was estimated on the basis of the land surface radiation balance:

$$R_n = SW_{\downarrow}\cdot(1-\alpha) + \varepsilon\cdot LW_{\downarrow} - \varepsilon\cdot\delta\cdot T_s^4 \quad (8)$$

where $SW_{\downarrow}$ (W/m^2) and $LW_{\downarrow}$ (W/m^2) are the at-surface downward solar radiation and downward thermal radiation, of which the daily values can be calculated by integrating the hourly ERA5 data, α is the surface albedo, ε is the land surface emissivity, δ is the Stefan-Boltzmann constant (5.67×10^{-8} W/m^2/K^4), T_s (K) is the daily mean surface temperature, which was assumed equal to the daily mean air temperature with soil surface heat flux equal to zero at daily scale.

In this study, the daily time series of ET and Rn at 1 km spatial resolution was estimated by applying the ETMonitor model with the reconstructed NDVI, albedo, downscaled ASCAT soil moisture, and the ERA5 meteorological reanalysis data.

For a heterogeneous region like the study area, the 1 km EF is still insufficient to capture the wetness conditions at the field scale. The ET and Rn can widely vary between cropland and the surrounding desert and crops with different phenology. Thus, a linear unmixing method was further applied to downscale the ET and Rn to 10 m, i.e., at the same spatial resolution as the crop map.

The linear unmixing procedure to downscale ET and Rn is based on the 10 m crop classification map. The 10 m classification map is used to define the endmembers. The procedure contains three general steps: (1) calculate the fractional abundance of each land use and crop (defined as endmembers) using the classification in each coarse grid (1 km); (2) obtain the ET and Rn of each endmember in the coarse grid data by linear unmixing (least square fit) within a moving window including 11 × 11 coarse grids as the first prediction of the 10 m ET and Rn of each endmember; (3) distribute homogeneously the coarse grid residual and update the ET and Rn estimation for each endmembers.

The basic assumption of the linear unmixing method is that the ET and Rn of each coarse grid C is the weighted sum of the values of each endmember within the same grid:

$$ET,\ R_n = \sum_{i=1}^{n} f_i\cdot c_i \quad (9)$$

where n is the number of endmembers, f_i is the areal fraction of class i within a coarse pixel, and c_i is the value of class i. This unmixing approach captures the general differences in ET and Rn between crops and the surrounding desert and among crop types with distinctive phenological characteristics, mixed in one coarse grid. On the other hand, it ignores the variability within the same crop types within the 11 × 11 coarse grids applied to solve Eq. (9). In other words, we assume that the spatial variability of ET and Rn within the nearby 11 × 11 coarse grids is only determined by the spatial variability of the fractional abundance of each land cover and crop type. Improvement in the results is expected by retrieving LST and estimating ET with satellite data at higher spatial resolution, such as Landsat 8/9 TIRS and SDGSAT-1 thermal infrared images in future work (Hair et al., 2018; Chen et al., 2022a).

3.7. Estimation of biomass and yield

The daily biomass (g/m^2/day) production is the result of the effective use of the absorbed solar energy, and limited by temperature and water stress:

$$Biomass = APAR\cdot\varepsilon_{max}\cdot f_T\cdot f_{H_2O} \quad (10)$$

where ε_{max} (g/MJ) is the maximum light use efficiency for biomass production, the value of which can be safely assumed to differ only between C3 and C4 crops according to Monteith (1972). In this study, we set ε_{max} to 2.5 g/MJ for C3 crops (i.e., wheat, sunflower, and melon) and 3 g/MJ for C4 crops (i.e., maize), based on literature, summarized in Bastiaanssen and Ali (2003).

The crop yield is formed through the partition of the total accumulated biomass of a plant to the marketable (yield related) plant parts. A simple description of this conversion is by applying the harvest index and the water content of the yield-related component to the estimated dry biomass so that the yield can be expressed as:

$$yield = \frac{H}{1-\theta}\sum_{e}^{h} Biomass \quad (11)$$

where H (dimensionless) is the harvest index, i.e., the fraction of the biomass accumulated during the growing season allocated to the yield-related plant organ, θ (dimensionless) denotes the water content in the yield-related plant organ, e and h represent the crop emergence and harvest date, respectively.

The harvest index and the water content are usually set to crop-specific values estimated on the basis of field experiments documented in literature (Bastiaanssen and Ali, 2003; Zwart et al., 2010). In this study, for spring wheat, maize, and sunflower, the harvest index was set to 0.35, 0.36, and 0.30 (Table 4), respectively, based on biomass measurements and growth analysis on plant samples conducted in the same study area (Chen et al., 2022b). The harvest index of melon was set to 0.64 based on the study of Huang et al. (2012). The grain water content of spring wheat and maize was set to 12.5% and 14%, respectively, according to the national moisture content standard for grain storage (Standardization Administration of the People's Republic of China, 2008, 2018). The local practice is to trade sunflower seeds after drying a few days after harvest, when the water content is reduced to around 25%. The water content of the local melon varieties is more variable (85%−90%) than that of cereals. In this study, the water content of sunflower and melon is set to 25% and 87%, respectively, as an approximation.

4. Results

4.1. Crop phenology at high spatial resolution

As illustrated in Fig. 3, clear differences exist in the estimated emergence and harvest dates of spring wheat, maize, sunflower, and melon, while the corresponding NDVI values (Table 5) are rather similar. This is, apparently due to the similar fractional ground cover associated with emergence and harvest, but attained at different moments in time. Our analysis showed the spatial variability in the NDVI temporal profiles for each crop was rather limited, thus supporting the method to estimate the NDVI threshold according to the typical emergence and harvest dates in the entire area. The north – south pattern in Fig. 4 is explained to a large extent by the spatial distribution of the main crops. Spring wheat, mainly located on the south of the oasis, shows the most distinctive phenology features with the earliest start of the growing season. The emergence date of wheat is generally in early April, as shown in Table 6. The harvest date for spring wheat is between late July to mid-August. For maize and sunflower, the emergence date is generally mid to late May. Maize has a longer growing season and a later harvest date than sunflower, which is generally till October. Among the four crops, melon, mainly located in the downstream desert-oasis

Table 4
The harvest index and the water content of the marketable product.

Crop type	Wheat	Maize	Sunflower	Melon
Harvest index (-)	0.35	0.36	0.3	0.64
Moisture content (%)	12.5	14	25	87

Table 5
NDVI thresholds to determine pixel-wise emergence and harvest dates for spring wheat, maize, sunflower, and melon.

Crop type	Wheat	Maize	Sunflower	Melon
Emergence	0.17	0.17	0.16	0.18
Harvest	0.36	0.40	0.34	0.31

Table 6
Spatial averages of the emergency and harvest dates (DOY) and their standard deviation (days) for spring wheat, maize, sunflower, and melon.

Crop type	Wheat	Maize	Sunflower	Melon
Emergence	99 (11)	138 (17)	144 (13)	154 (18)
Harvest	209 (13)	270 (12)	255 (14)	262 (14)

region, shows the latest emergence date at the beginning of June. This is related to the relatively higher temperature requirement for the seed gemination of melon plants (Saberali and Shirmohamadi-Aliakbarkhani, 2020). Generally, the spatial variability in the emergence and harvest dates of each crop is moderate (Table 6), while the local phenological knowledge does not give any spatial variability on crop phenology.

4.2. PAR and fAPAR

The value of fAPAR is linearly related to NDVI (Eq. (2)) and gradually changes during the growth of vegetation. Fig. 5 displays the fAPAR values for the spring wheat, maize, sunflower, and melon on days from mid of April to September as an example. For spring wheat, fAPAR reaches the maximum value in mid-June. The fAPAR maximum is in July for sunflower and August for maize and melon. In the peak month, when green vegetative parts are fully developed, fAPAR was around 0.8 for spring wheat, maize, and sunflower, and 0.6 for melon. The lower peak for melon is caused by the lower planting density and limited vertical plant development.

Fig. 6 illustrates the spatially averaged daily PAR estimated using the ERA5 meteorological hourly data. The upper envelope of the PAR time series (Fig. 6) suggests a potential seasonal trend under clear sky conditions. In the middle of the growth cycle, the daily value of PAR under clear sky can reach 160 W/m^2, equivalent to 13.8 MJ/m^2/day. In the SRB, in summer, drier air, higher solar radiation, longer sunshine duration, and larger daily amplitude of air temperature are favorable conditions for high yield agriculture. The troughs in Fig. 6 correspond to cloudy conditions, where the value of PAR can decrease to 40 W/m^2, equivalent to 3.45 MJ/m^2/day. Because of such a big gap, daily PAR is required to estimate the accumulated biomass and the final yield.

4.3. Air temperature stress factor

The daily mean T_a, required to determine f_{T_1} and f_{T_2}, is estimated as described in Sect. 3.4. We established a linear relationship between T_a and LST for each station separately and for all stations together. The results (Table 7) show that MODIS LST and T_a observations are linearly related with R (the correlation coefficient) varying between 0.77 to 0.87. The m, n, and R in Eq. (6) in the relationships for each specific station and the ones for all stations did not differ significantly. This implies the possibility of using a single equation for the whole study area. Adopting the same relationship for the entire area only leads to an increment of RMSE on estimated air temperature between 0.3% and 5.2%, with MAE between 0% and 9.2% (Table 8). Because of these results, the relationship for all stations in Table 7 (m = 0.94 and n = -13.38) was applied over the whole study area to estimate the pixel-wise daily mean T_a.

As illustrated in Fig. 7, the spatial pattern of T_a with spatial resolution of 1 km successfully reflects the distinctive thermal characteristic of different land covers and terrain elevation in the SRB. The cold mountain region shows the lowest T_a, i.e., $T_a < 10$ °C even in summer for most of the region. Most important, the T_a map captures rather well the finer details of the temperature variability within the oases and within the desert, in addition to the broad desert-oasis temperature pattern. The lower air temperature of narrow irrigated patches is clearly observable in the 1 km T_a map. In the desert area, daily mean T_a can be larger than 35 °C. In the oasis region, under the influence of irrigation, T_a is significantly lower than the surrounding desert, i.e., between 15 °C and 25 °C in the growing season.

The temperature stress factor f_{T_1} (Eq. (4)) expresses a regulation of temperature on plant growth for extremely cold or hot climates. f_{T_1} varies with the optimal temperature, and does not change with time. The

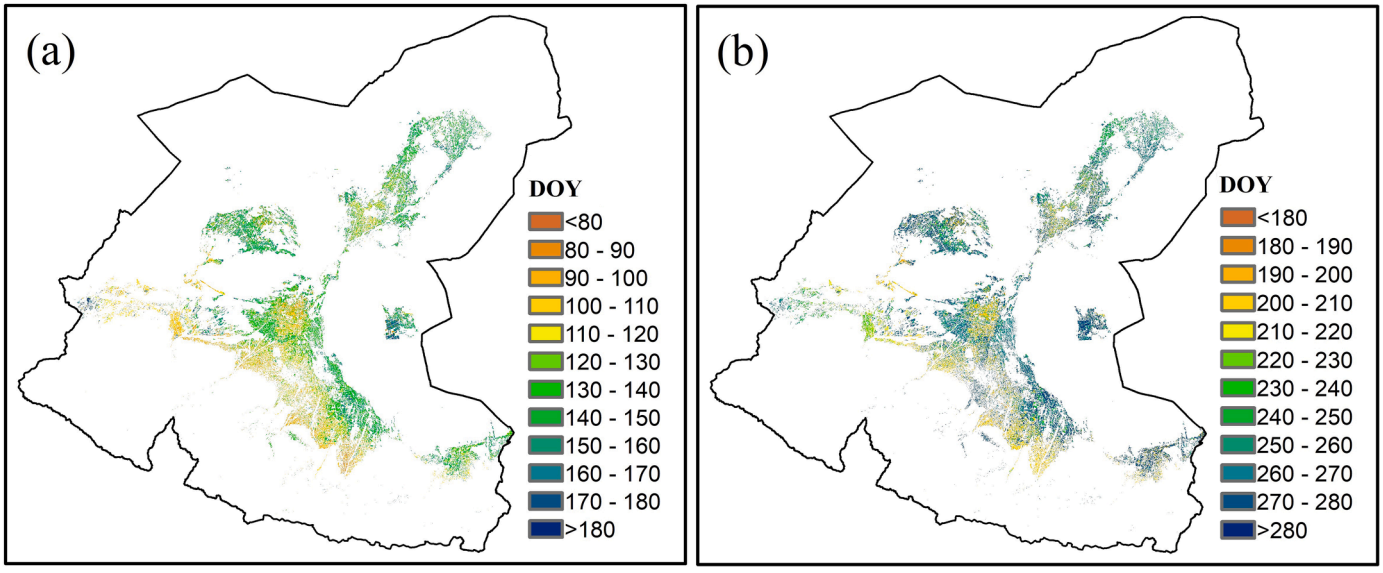

Fig. 4. Pixel-wise crop emergence (a) and harvest (b) date in the SRB of croplands in 2019.

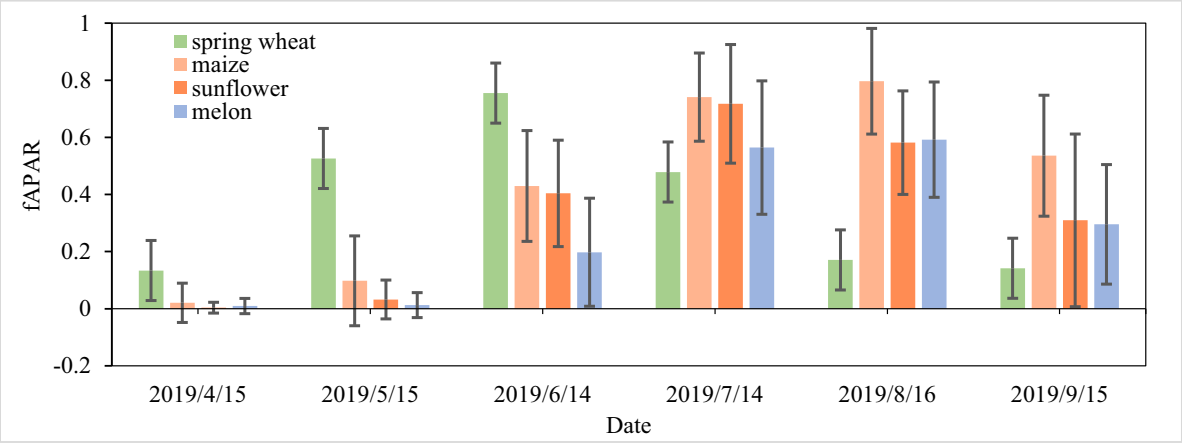

Fig. 5. Mean fAPAR and its standard deviation in space for spring wheat, maize, sunflower, and melon in the SRB in 2019.

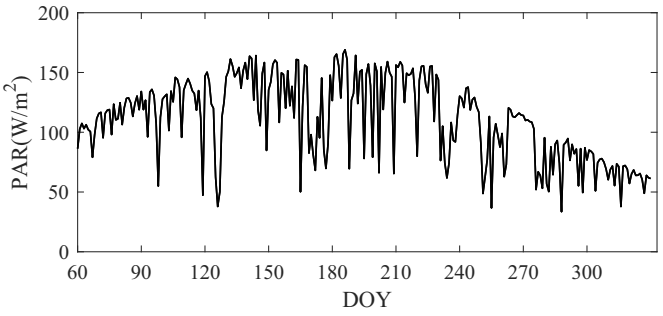

Fig. 6. The spatially averaged daily PAR time series in the Shiyang river basin in 2019.

Table 7
Statistics of the linear regression parameters (m, n) and correlation coefficient (R) calculated at the available meteorological stations in the SRB.

Station	m	n	R
Minqin	0.99	-13.80	0.81
Wuwei	0.91	-13.45	0.77
Jinchang	0.92	-12.77	0.87
All stations	0.94	-13.38	0.81

results show that the mean f_{T_1} in the cropland in the SRB is as high as 0.98 – 1.0 with a standard deviation of less than 0.02, which indicates that the local climate is suitable for agriculture. The temperature stress factor f_{T_2} (Eq. (5)) parameterizes how a plant adapts to the local climate. With the application of f_{T_2}, the LUE is reduced when the air temperature is either lower or higher than the local optimal temperature. The f_{T_2} for wheat, maize, sunflower, and melon during April to September (Fig. 8) is always larger than 0.91 (the deviation less than 0.06) with a seasonal trend following crop phenology.

4.4. Water stress factor

As described in Sect. 3.5, an RF machine-learning model was applied to obtain a spatially continuous soil moisture dataset with high spatial resolution using the gap-filled MODIS LST, NDVI, and albedo, SRTM DEM, longitude, and latitude as covariates. The trained RF model is well calibrated with a low RMSE of 0.06 and a high R^2 of 0.92. In the original ASCAT map (e.g., Fig. 9a), the spatial details of soil moisture are clearly blurred. However, the main differences in soil moisture among oases, desert, and mountain vegetation are observable. Moreover, the comparison of Fig. 9a and 9b reveals that the downscaled soil moisture is consistent with the details of desert-oasis pattern. Within the south oasis, clear differences in soil moisture were observable and explained by the crop pattern. ET and Rn were further downscaled based on the method introduced in Sect. 3.6 and used to estimate the water stress factor. Fig. 9d gives an example of the water stress factor on 16th Aug, indicating a range between 0.3 and 1.0. Generally, water stress is more serious in the north SRB than the south due to less water availability, as indicated by the downscaled soil moisture. In addition, the wheat area (refer to Fig. 1c) shows more severe water stress, since, in August, most of wheat had been harvested already. The observed differences in downscaled soil moisture and water stress indicator between the

Table 8
RMSE and MAE and their relative increment in the estimates of T_a using station-specific linear regressions and a single linear regression.

Stations	Station specific		All stations		Increment of relative error	
	RMSE (°C)	MAE (°C)	RMSE (°C)	MAE (°C)	RMSE	MAE
Minqin	3.60	2.94	3.79	3.21	5.2%	9.2%
Liangzhou	3.62	2.93	3.74	3.14	3.3%	7.2%
Jinchang	2.91	2.31	2.92	2.31	0.3%	0

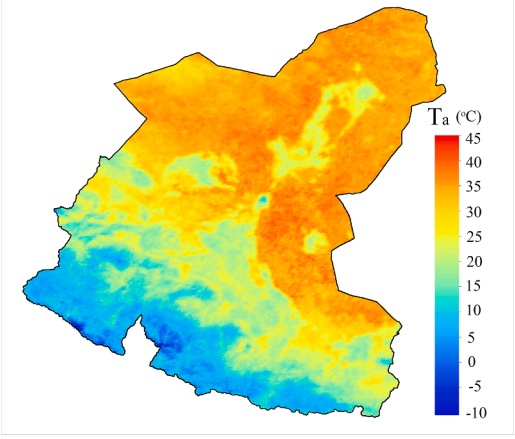

Fig. 7. Spatial variability of daily mean T_a in Jul. 14 2019 in the SRB.

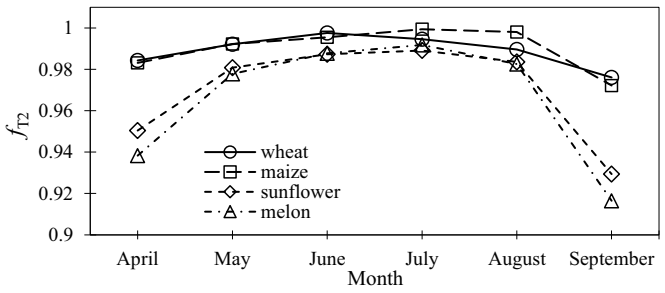

Fig. 8. Monthly temperature stress factor f_{T_2} for wheat, maize, sunflower, and melon in the SRB based on data in 2019.

northern and southern oasis are consistent with the allocation of irrigation water, which tends to favor the southern oasis.

4.5. Accumulated biomass and yield estimation

Accumulated biomass in the maize-producing region (Fig. 10) exhibits higher values compared with the other crops. The biomass of wheat (Fig. 11) grows up earlier, consistently with the early growing season. The stage of rapid increase in biomass, i.e., higher photosynthesis rate, is from May to June for wheat, and June to August for the other crops. For C3 crops, i.e., wheat, sunflower, and melon, the mean value of accumulated biomass is between 1000–1500 g/m^2. The relatively lower biomass accumulation of melon, compared with wheat and sunflower, is related to its shorter growing season and lower planting density. For maize, as a C4 crop type with a higher LUE, the mean biomass increases more rapidly and can reach over 2000 g/m^2 at the end of the growing season.

By specifying the harvest index and moisture content (see Sect. 3.7) for each crop type, the accumulated biomass can be converted to the final yield (Fig. 13). At basin level, the estimated yields of wheat and maize are 6.87 and 8.53 t/h, respectively, which are very comparable with the officially reported data in the Gansu Development Yearbook 2020. The relative errors for the two main grain crops compared to the census data are less than 5% (Table 9). At the county level, the estimated wheat yields of Liangzhou, Minqin, Gulang, Jinchuan, and Yongchang are 6.07, 5.20, 5.40, 5.55, and 6.95 t/ha, respectively, with relative errors equal to 0.87%, 24.2%, 9.7%, 12.5%, and 7.2% (Fig. 12). For maize, the estimated yields in Liangzhou, Minqin, Jinchuan, Yongchang, and Gulang are 8.86, 7.18, 8.87, 8.25, and 8.22 t/ha. The relative errors for maize yield compared with the census data in Liangzhou, Minqin, Jinchuan, and Yongchang are less than 5%. In Gulang, the relative error is up to 40%. The exact reason for the gap in Gulang has not been found. There is no sign that the growth of maize in Gulang county is under higher stress from remote sensing signals (e.g., the value of NDVI). The Gulang census data for maize yield is more variable during 2014 – 2019, ranging from 5.98 to 9.95 t/ha. Accordingly, this gap may be partly due to a poorer representativeness of the samples used in the census data and the unsuitable setting of the local harvest index in the model. To evaluate the estimated yield of sunflower, which is missing in the official census data, yield data from field interviews in Minqin county has been used. These fields have received a better nutrient and water supply. The relative error of the estimated sunflower yield (6.38 t/ha) deviates by 5% from the real yield (6.0 t/ha). Since only the regional total yield of melon and other fruits has been recorded in the officially reported data,

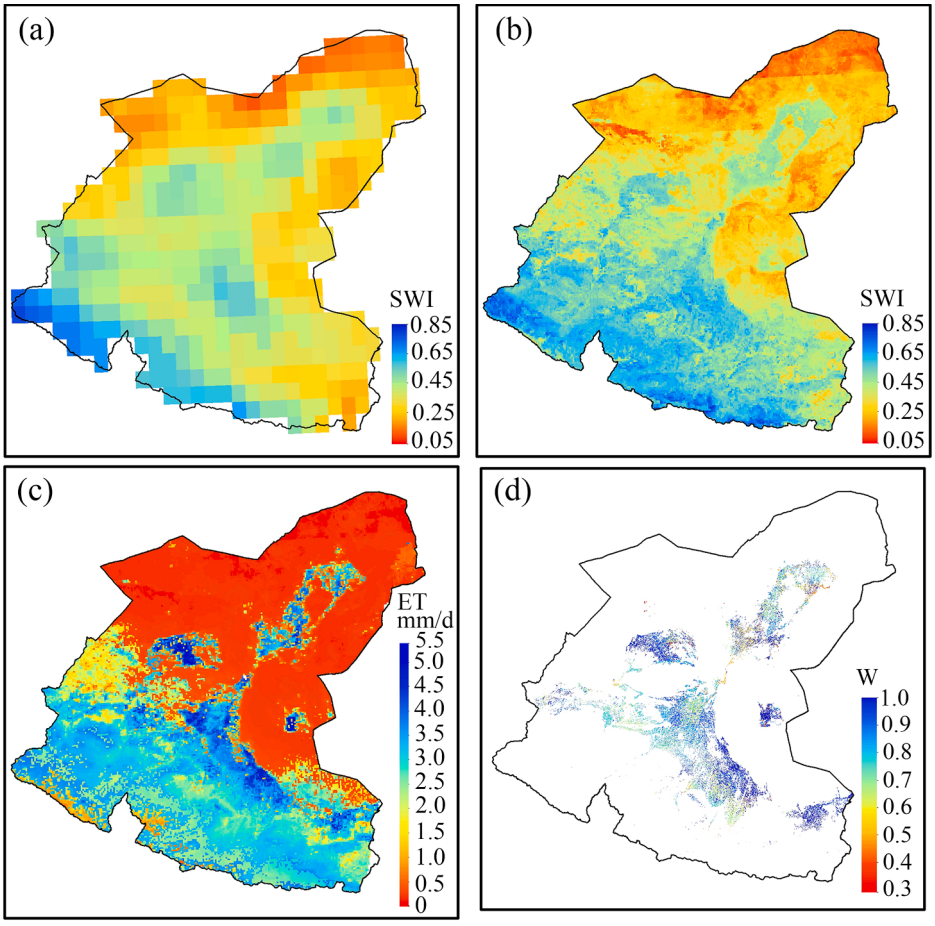

Fig. 9. Original ASCAT soil moisture at 10 km resolution (a), downscaled soil moisture at 1 km (b), the corresponding ET (c) estimated using the downscaled soil moisture, and the water stress factor at 10 m (d) in the SRB on Aug. 16th, 2019.

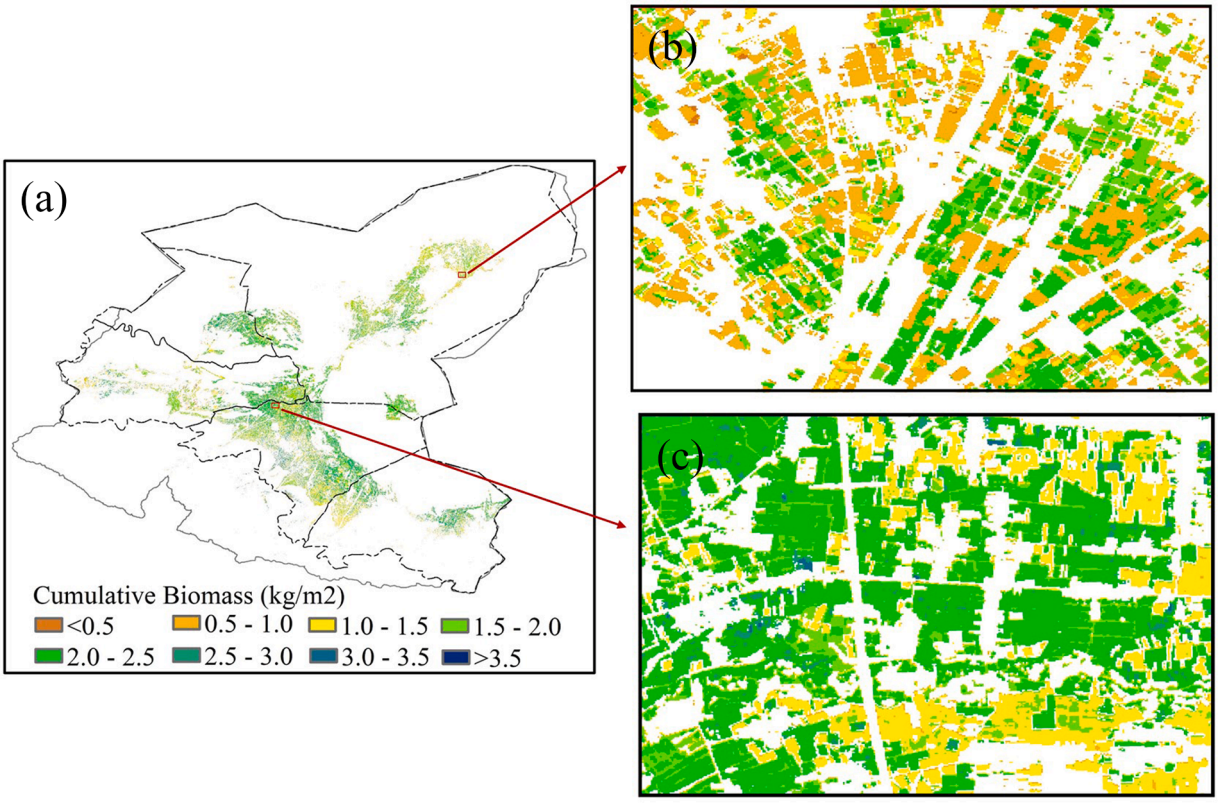

Fig. 10. Spatial distribution of accumulated biomass in croplands in the SRB in 2019 (a), and (b) and (c) are full 10 m resolution maps of the areas shown in Fig. 1d and 1e.

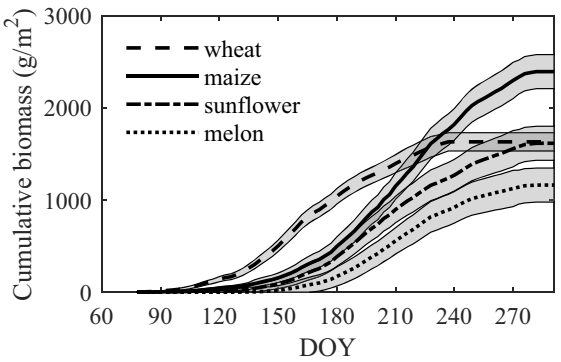

Fig. 11. Spatially averaged accumulated biomass for wheat, maize, sunflower, and melon during the growing season in the SRB in 2019; the shaded areas indicate the spatial variability with a range equal to ± one standard deviation.

the validation of melon yield has been done only in the Minqin county, where fruits other than melon only account for a very small portion. The relative error of the estimated melon yield (52.24 t/ha) is 16%, compared with the officially reported yield (44.93 t/ha).

5. Discussion

The modeling approach developed in this study was conceived to describe the response of highly heterogeneous desert-oasis system to climate variability and land and water management. The issues to be addressed were: a) the spatial variability in crop phenology; b) the spatial variability in crop conditions and their impact on absorption of photosynthetic light; c) the larger contrast in thermal conditions between desert and oases and within the oases; d) the spatial variability of available soil water and its dependence on irrigation; e) the temporal and spatial variability, modulated by soil and growth conditions, of crop response to available soil water and f) the relationship between biomass and marketable yield.

5.1. Crop phenology

In crop-growth dynamic models, the phenology, namely the emergence and harvest dates, is usually determined by a set of temperature sums (thermal times), associated with each phenological stage (Hijmans et al., 1994). To calculate temperature sums, a reference (baseline) temperature must be known for each crop, likewise the values of temperature sums associated with each phenological stage and each crop. This approach is difficult to apply in the case of the desert-oasis agroecosystem addressed by this study for a two-fold reason: the extreme sparseness of the meteorological stations in the oases and the absent knowledge on the baseline temperature and the thermal times. Accordingly, we explored an alternate approach: see Sect. 3.2 for a detailed description. This method considers the specific characteristics of different crops and makes effective use of limited local phenological knowledge to determine the NDVI thresholds at the emergence and harvest dates in the growing season. The core assumption is the spatial variability in the temporal NDVI profiles does not modify completely their shape, so that the thresholds estimated on the average NDVI profiles are applicable to the pixel-wise profiles. If local phenological observations were available, the emergence and harvest dates could be estimated on the basis of the temperature sums applying to each phenological stage, then the corresponding NDVI values would retain the spatial variability of the temperature sums. This would lead to an even finer description of crop phenology, avoiding the use of the same NDVI threshold in the entire area.

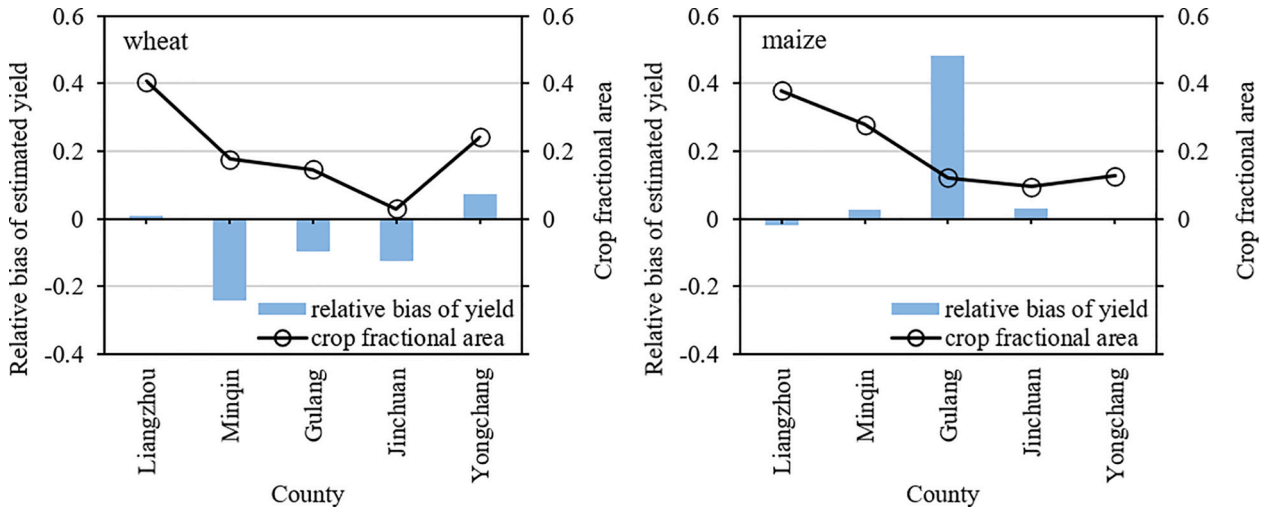

Fig. 12. Relative bias on yield (blue bars, left axis) and the fractional areas (black line with dot, right axis) of wheat (a) and maize (b) at county level in the SRB, 2019; fractional areas are fractions of the total area of each crop in the five counties.

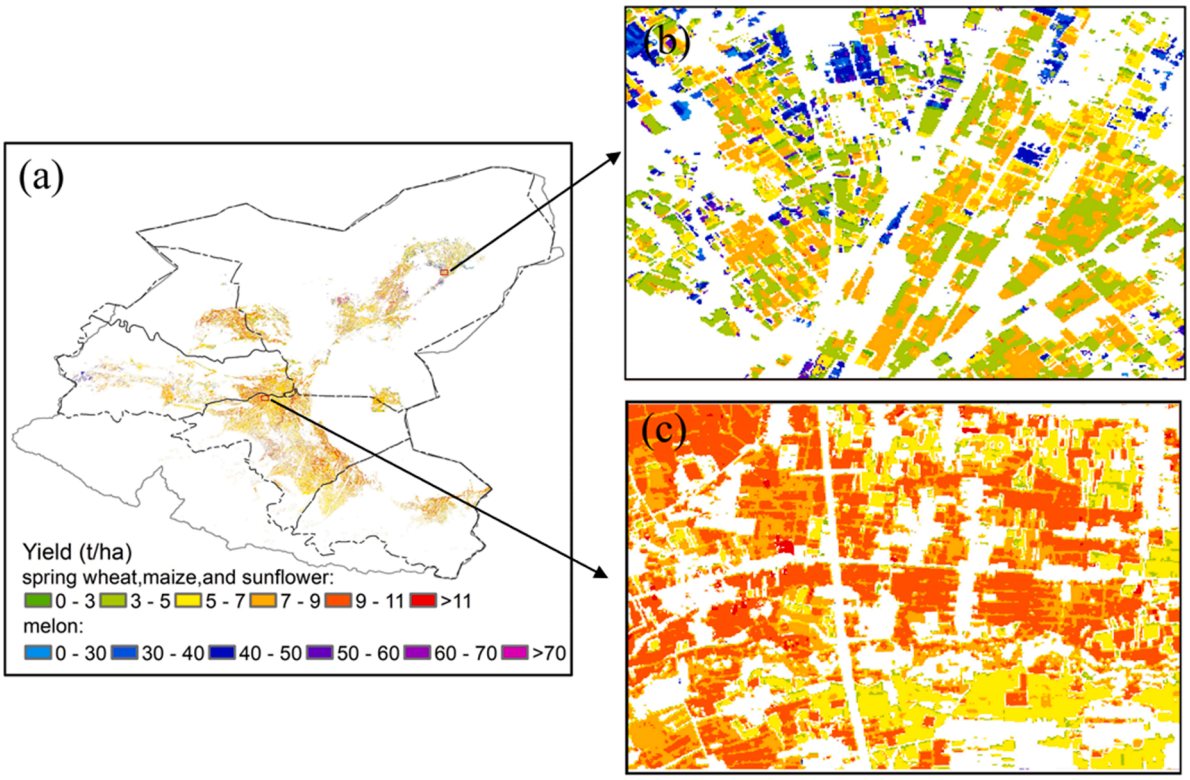

Fig. 13. Spatial distribution of crop yield in the SRB, 2019 (a), (b) and (c) are full 10 m resolution yield maps of the areas shown in Fig. 1d and 1e.

Table 9
Accuracy of the estimated yields of wheat and maize at basin level of the SRB compared with the census data.

Crop type	Estimated yield ± standard deviation (t/ha)	Census (t/ha)	Bias (t/ha)	Relative difference (%)
Wheat	5.87 ± 1.3	6.11	-0.24	3.9
Maize	8.53 ± 1.93	8.31	0.22	2.6

5.2. Absorption of photosynthetic light (fAPAR)

The efficiency of the absorption of the PAR is determined by the concentration and type of leaf pigments, which vary significantly depending on varieties, fertilization, and more in general crop conditions. This spatial and temporal variability is hard to capture, without the support of multi-spectral remote sensing, although it is an essential element of LUE-based modeling of biomass accumulation and crop yield. To this purpose, we applied multi-spectral images at high spatial resolution. A wealth of studies explored the relationship between fAPAR and NDVI (Daughtry et al., 1992; Myneni and Williams, 1994; Chen, 1996; Gitelson et al., 2014). We use the linear equation proposed in Bastiaanssen and Ali (2003), as applicable to multiple crops including the ones in the SRB. Quantitative remote sensing measurements can be interpreted with the support of radiative transfer modeling in vegetation canopies to obtain generalized relationships between spectral reflectance and fAPAR (Goward and Huemmrich, 1992). Field-scale

experiments by Tedeschi et al. (2011) and Tedeschi et al. (2017) showed that the melon crop yield under saline-sodic stress, will be reduced due to the decreasing leaf area and biomass production. These studies imply that the estimation of fAPAR can be further improved by considering field-scale soil conditions.

5.3. Thermal conditions

In a desert and oasis landscape, thermal heterogeneity of the land surface and the local variation of air temperature is not negligible, as a consequence of the large variability in hydrological conditions between the desert and the oases and within the oases. Proper characterization of spatial and temporal variability of thermal conditions is a critical aspect of a broad range of ecosystems. For regional-scale applications, air temperature is usually interpolated from the meteorological ground stations or provided by reanalysis datasets (with grid resolution at 0.1 - 0.5°). Neither of these solutions would capture the details of water related thermal conditions in the oases of the SRB. Land surface temperature is a measure of the local equilibrium in heat fluxes in response to water conditions. This leads to using LST as a predictor of air temperature, as done in this study. The estimation of air temperature is affected by not negligible errors (Table 8), but still relatively small compared with the large difference between oases and desert, i.e., 15–25 °C as noted (Fig. 7). Possible improvements in future studies include the use of additional periodic components in the HANTS time series reconstruction or the use of the different method for this purpose, and the use of a denser network of weather stations if available.

5.4. Available soil water

In the SRB, as in any irrigated area, the soil water is largely determined by irrigation. Accurate and detailed data on actually applied irrigation water are rarely available and the use of remote sensing retrievals of soil water content is gaining support (Zaussinger et al., 2019). In the SRB, serious water conflicts exist between ecosystem preservation and agriculture and between different irrigation zones. In the oases, water availability varies and irrigation time is different for crops with different phenology. Thus, in this study, we applied remotely sensed soil moisture to account for the application of irrigation water. The extraction of information from microwave data, capturing the water conditions, is frequently hampered by low spatial resolution, i.e., 10 km – 25 km. Such kind of resolution cannot capture the heterogeneity in soil water conditions within the oases and the sharp contrast at the oasis-desert boundary. This is then a two-fold problem: a) soil water content must be estimated at a spatial resolution consistent with the heterogeneity of the irrigated oases and b) the root zone soil water content must be estimated. The latter issue is addressed in the next paragraph in relation to the ETMonitor system. To address the first issue, we first evaluated candidate soil water condition data products to conclude that in 2019 only the ASCAT data product could capture the main features of the pattern in soil water determined by irrigation in the oases (Fig. 10). To downscale the ASCAT data product, we identified multiple candidate covariates to develop a multi-dimensional machine-learning model. The covariates are the drivers of the spatial pattern of soil moisture, i.e., vegetation, soil surface temperature, albedo, and elevation (see Sect. 3.5). As shown in Sect. 4.4, this model could be accurately calibrated, and delivers estimates of soil water content at 1 km spatial resolution, which is sufficient to distinguish soil water conditions in the broad irrigated and not irrigated patches within the oases (Fig. 9b).

5.5. Crop response to available soil water

Soil water availability determines the rapid crop response through the regulation on the stomatal conductance and therefore efficiently influence the carbon assimilation efficiency. This response is determined by soil conditions, canopy characteristics, and the meteorological conditions expressed by the difference between actual and potential ET. Actual ET was estimated with ETMonitor (Sect. 3.6) using a suite of remote sensing observations, including soil available water as described above. In this way, actual ET includes the contribution of irrigation water, i.e., it reflects the actual irrigation water depths. This is done by estimating the root zone soil water content using a parameterization based on the top soil water content (see Sect. 3.5) and NDVI (Hu and Jia, 2015). The accuracy of ETMonitor has been documented against eddy covariance measurement of ET at a number of sites worldwide, to yield an overall RMSE equal to 0.93 mm/day and R equal to 0.75, applying to multiple cropland sites (Zheng et al., 2022). The downscaling procedure described (Sect. 3.6) assumes that the actual ET of each crop type does not change within each moving window (11 x 11 km^2). This notwithstanding, the higher resolution ET captures correctly the differences between irrigated and not irrigated patches, as for example between wheat and maize fields in the southern oasis on Aug. 16th (Fig. 9d). A different solution to obtain high resolution estimates of available soil water and actual ET will be offered by a new version of ETMonitor, which uses land surface temperature rather than microwave radiometry to characterize soil and water conditions. This version makes use of LST observations at higher spatial resolution such as Landsat 8/9 TIRS and SDGSAT thermal infrared images (Hair et al., 2018; Chen et al., 2022a).

5.6. Biomass and marketable yield

Harvest index and the maximum LUE are the most significant calibration parameters. For each crop, both harvest index and maximum LUE are relatively well known to vary within a certain range (Bastiaanssen and Ali, 2003; Zwart et al., 2010). For grain crops, it is usually accepted that the harvest index within the same climate zone is fairly stable for a specific crop due to the high heritability, unless severe stresses from nutrient, extreme weather, and water occur (Hay, 1995). The well-simulated wheat and maize yields prove the rationality of the fixed harvest index in the study area. For melon, the harvest index is more variable between different melon varieties and environmental stress can reduce the potential harvest index. Huang et al. (2012), in the same study area, showed that the melon harvest index can increase significantly with increasing salinity of irrigation water. This influence should be further studied. As regards the limitations in growth rate, besides temperature and soil water stress, various models integrate the dependence on vapor pressure deficit, atmospheric CO_2 concentration, diffuse radiation ratio, etc. (Running et al., 2000; Veroustraete et al., 2002; He et al., 2013; Zhang et al., 2016). These models are designed to better account for climate forcing, plant physiology, and canopy structure in vegetation productivity but have rather demanding data requirements.

In the SRB, water security depends largely on melt water from the Qilian mountains, while food security and sustainable development in the region require equitable water allocation between the southern and northern oasis. The model described in this study could be useful to support monitoring of agroecosystem services towards water and food security.

It should be noted that the issues discussed above apply to a broad range of agroecosystems, particularly the fragmentation of land use and the resulting heterogeneity of crop and water conditions. The solutions we developed and applied in this study of the SRB, therefore, are relevant to a broader range of land and water systems than the desert-oasis in the SRB. Particularly, the procedures applied to replace detailed local data on crop conditions, soil water availability, and crop response to water stress are effective solutions to take advantage of the information conveyed by remote sensing observations. This concept fits neatly in the argument of Jones et al. (2017), who emphasized that data scarcity is even more important than theory limitations in agricultural monitoring and forecast.

6. Conclusions

The modeling approach developed in this study was conceived to describe the response of highly heterogeneous desert-oasis system to climate variability and land and water management. The modeling system at high spatial resolution is applicable to a broad range of agroecosystems, particularly to deal with the fragmentation of land use and the resulting heterogeneity of crop and water conditions. The solutions we developed and applied in this study of the SRB, therefore, are relevant to a broader range of land and water systems than the deser-oasis in the SRB. Particularly, the procedures applied to replace detailed local data on crop conditions, soil water availability, and crop response to water stress are effective solutions to take advantage of the information conveyed by remote sensing observations.

Crop yield estimation in heterogeneous regions is challenging due to the gaps in local data. The problems of both data continuity in space and time and the scaling issue were considered. In general, the continuous change of crop conditions at field scale during the growing season has been well captured. As regards soil properties, soil moisture, and environmental conditions, e.g., the air temperature, the data gaps are mitigated by applying data fusion and downscaling. The evaluation of estimated crop yield against official census data and field interviews proves the reliability of the LUE based model and the data processing we applied. Knowledge on soil type and conditions, especially on soil salinity, would improve the estimation of crop response to water in water limited region.

CRediT authorship contribution statement

Qiting Chen: Conceptualization, Methodology, Software, Validation, Investigation, Formal analysis, Visualization, Supervision, Funding acquisition, Data curation, Resources, Writing – original draft, Writing – review & editing. **Li Jia:** Conceptualization, Methodology, Investigation, Supervision, Data curation, Funding acquisition, Resources, Writing – review & editing. **Massimo Menenti:** Conceptualization, Methodology, Resources, Writing – review & editing. **Guangcheng Hu:** Conceptualization, Methodology, Writing – review & editing. **Kun Wang:** Conceptualization, Methodology. **Zhiwei Yi:** Methodology, Investigation, Data curation. **Jie Zhou:** Methodology. **Fei Peng:** Investigation, Methodology. **Shaoxiu Ma:** Conceptualization, Project administration, Resources. **Quangang You:** Investigation. **Xiaojie Chen:** Investigation. **Xian Xue:** Conceptualization, Investigation, Resources.

Declaration of Competing Interest

The authors declare that they have no known competing financial interests or personal relationships that could have appeared to influence the work reported in this paper.

Data availability

The remote sensing and reanalysis data products are publicly available. The authors do not have permission to share the meteorological in-site data.

Acknowledgments

This work is jointly supported by the National Key Research and Development Plan of China (Grant no. 2017YFE0119100), the Strategic Priority Research Program of the Chinese Academy of Sciences (Grant no. XDA19030203), the Natural Science Foundation of China (Grant no. 41805013), the Chinese Academy of Sciences President's International Fellowship Initiative (Grant no. 2020VTA0001), the MOST High Level Foreign Expert program (Grant no. G2022055010L), and the European Union's Horizon 2020 research and innovation program (Grant no. 776848).

References

Alfieri, S.M., De Lorenzi, F., Menenti, M., 2013. Mapping air temperature using time series analysis of LST: the SINTESI approach. Nonlinear Process Geophys. 20 (4), 513–527. https://doi.org/10.5194/npg-20-513-2013.

Bastiaanssen, W.G.M., Ali, S., 2003. A new crop yield forecasting model based on satellite measurements applied across the Indus Basin, Pakistan. Agriculture Ecosyst. Environ. 94 (3), 321–340. https://doi.org/10.1016/S0167-8809(02)00034-8.

Breiman, L., 2001. Random forests. Mach. Learn. 45 (1), 5–32. https://doi.org/10.1023/A:1010933404324.

Chen, J., et al., 2022a. A TIR-visible automatic registration and geometric correction method for SDGSAT-1 thermal infrared image based on modified RIFT. Remote Sens. 14 (6), 1393. https://doi.org/10.3390/rs14061393.

Chen, J.M., 1996. Canopy architecture and remote sensing of the fraction of photosynthetically active radiation absorbed by boreal conifer forests. IEEE Trans. Geosci. Remote Sens. 34 (6), 1353–1368. https://doi.org/10.1109/36.544559.

Chen, X.J., et al., 2022b. Irrigation quotas for high water use efficiency and economic water productivity of typical crops in Shiyang River Basin. Chinese J. Appl. Environ. Biol. https://doi.org/10.19675/j.cnki.1006-687x.2021.05041.

Cui, Y., Jia, L., 2021. Estimation of evapotranspiration of "soil-vegetation" system with a scheme combining a dual-source model and satellite data assimilation. J. Hydrol. (Amst) 603, 127145. https://doi.org/10.1016/j.jhydrol.2021.127145.

Daughtry, C.S.T., Gallo, K.P., Goward, S.N., Prince, S.D., Kustas, W.P., 1992. Spectral estimates of absorbed radiation and Phytomass production in corn and soybean canopies. Remote Sens. Environ. 39 (2), 141–152. https://doi.org/10.1016/0034-4257(92)90132-4.

de Wit, A.J.W., van Diepen, C.A., 2007. Crop model data assimilation with the Ensemble Kalman filter for improving regional crop yield forecasts. Agric. For. Meteorol. 146 (1–2), 38–56. https://doi.org/10.1016/j.agrformet.2007.05.004.

Field, C.B., Randerson, J.T., Malmstrom, C.M., 1995. Global net primary production - combining ecology and remote-sensing. Remote Sens. Environ. 51 (1), 74–88. https://doi.org/10.1016/0034-4257(94)00066-V.

Gansu Development Yearbook Editorial Committee, 2021. Gansu Development Yearbook 2020. China Statistics Press, Beijing.

Gao, X.J., Giorgi, F., 2008. Increased aridity in the Mediterranean region under greenhouse gas forcing estimated from high resolution simulations with a regional climate model. Glob. Planet. Change 62 (3–4), 195–209. https://doi.org/10.1016/j.gloplacha.2008.02.002.

Gitelson, A.A., Peng, Y., Huemmrich, K.F., 2014. Relationship between fraction of radiation absorbed by photosynthesizing maize and soybean canopies and NDVI from remotely sensed data taken at close range and from MODIS 250m resolution data. Remote Sens. Environ. 147, 108–120. https://doi.org/10.1016/j.rse.2014.02.014.

Goetz, S.J., Prince, S.D., Small, J., Gleason, A.C.R., 2000. Interannual variability of global terrestrial primary production: results of a model driven with satellite observations. J. Geophys. Res. Atmos. 105 (D15), 20077–20091. https://doi.org/10.1029/2000jd900274.

Goward, S.N., Huemmrich, K.F., 1992. Vegetation canopy par Absorptance and the normalized difference vegetation index - an assessment using the sail model. Remote Sens. Environ. 39 (2), 119–140. https://doi.org/10.1016/0034-4257(92)90131-3.

Gower, S.T., Kucharik, C.J., Norman, J.M., 1999. Direct and indirect estimation of leaf area index, fAPAR, and net primary production of terrestrial ecosystems. Remote Sens. Environ. 70 (1), 29–51. https://doi.org/10.1016/s0034-4257(99)00056-5.

Hadipour, M., 2021. Geospatial modeling of landscape ecological sustainability level in geo-tourism regions. Scientific Reports in Life Sci. 2 (1), 58–72. https://doi.org/10.22034/srls.2021.522674.1011.

Hair, J.H., et al., 2018. Landsat 9 thermal infrared sensor 2 architecture and design, 38th IEEE international geoscience and remote sensing symposium (IGARSS). In: IEEE International Symposium on Geoscience and Remote Sensing IGARSS. IEEE, pp. 8841–8844.

Haxeltine, A., Prentice, I.C., 1996. A general model for the light-use efficiency of primary production. Funct. Ecol. 10 (5), 551–561. https://doi.org/10.2307/2390165.

Hay, R.K.M., 1995. Harvest index - a review of its use in plant-breeding and crop physiology. Ann. Appl. Biol. 126 (1), 197–216. https://doi.org/10.1111/j.1744-7348.1995.tb05015.x.

He, M.Z., et al., 2013. Development of a two-leaf light use efficiency model for improving the calculation of terrestrial gross primary productivity. Agric. For. Meteorol. 173, 28–39. https://doi.org/10.1016/j.agrformet.2013.01.003.

Hijmans, R.J., Lens, I.M.G., Diepen, C.A.V., 1994. WOFOST 6.0: User's Guide For the WOFOST 6.0 Crop Growth Simulation Model. DLO Winand Staring Centre, Wageningen.

Holzworth, D.P., et al., 2014. APSIM – Evolution towards a new generation of agricultural systems simulation. Environ. Modell. Software 62, 327–350. https://doi.org/10.1016/j.envsoft.2014.07.009.

Hu, G.C., Jia, L., 2015. Monitoring of evapotranspiration in a semi-arid inland river basin by combining microwave and optical remote sensing observations. Remote Sens. 7 (3), 3056–3087. https://doi.org/10.3390/rs70303056.

Huang, C.H., et al., 2012. Impact of saline water irrigation on yield and quality of melon (Cucumis melo cv. Huanghemi) in northwest China. Eur. J. Agron. 43, 68–76. https://doi.org/10.1016/j.eja.2012.05.008.

Huang, J.X., et al., 2019. Assimilation of remote sensing into crop growth models: current status and perspectives. Agric. For. Meteorol. 276. https://doi.org/10.1016/j.agrformet.2019.06.008.
Jin, X.L., et al., 2018. A review of data assimilation of remote sensing and crop models. Eur. J. Agron. 92, 141–152. https://doi.org/10.1016/j.eja.2017.11.002.
Jones, J.W., et al., 2017. Toward a new generation of agricultural system data, models, and knowledge products: state of agricultural systems science. Agric. Syst. 155, 269–288. https://doi.org/10.1016/j.agsy.2016.09.021.
Jones, J.W., et al., 2003. The DSSAT cropping system model. Eur. J. Agronomy 18 (3–4), 235–265. https://doi.org/10.1016/s1161-0301(02)00107-7.
Li, W.D., Li, Z.Z., Wang, J.Q., 2007. Evaluation of oasis ecosystem risk by reliability theory in an and area: a case study in the Shiyang River Basin, China. J. Environ. Sci. 19 (4), 508–512. https://doi.org/10.1016/s1001-0742(07)60085-0.
Liu, D., Mishra, A.K., Yu, Z.B., 2019. Evaluation of hydroclimatic variables for maize yield estimation using crop model and remotely sensed data assimilation. Stochastic Environ. Res. Risk Assessment 33 (7), 1283–1295. https://doi.org/10.1007/s00477-019-01700-3.
McCree, K.J., 1972. Test of current definitions of photosynthetically active radiation against leaf photosynthesis data. Agricultural Meteorol. 10, 443–453. https://doi.org/10.1016/0002-1571(72)90045-3.
Menenti, M., Azzali, S., Verhoef, W., van Swol, R., 1993. Mapping agroecological zones and time lag in vegetation growth by means of fourier analysis of time series of NDVI images. Adv. Space Res. 13 (5), 233–237. https://doi.org/10.1016/0273-1177(93)90550-u.
Monteith, J.L., 1972. Solar-radiation and productivity in tropical ecosystems. J. Appl. Ecol. 9 (3), 747–766. https://doi.org/10.2307/2401901.
Myneni, R.B., Williams, D.L., 1994. On the relationship between Fapar and Ndvi. Remote Sens. Environ. 49 (3), 200–211. https://doi.org/10.1016/0034-4257(94)90016-7.
Potter, C.S., et al., 1993. Terrestrial ecosystem production - a process model-based on global satellite and surface data. Global. Biogeochem. Cycles 7 (4), 811–841. https://doi.org/10.1029/93gb02725.
Roerink, G.J., Menenti, M., Verhoef, W., 2000. Reconstructing cloudfree NDVI composites using Fourier analysis of time series. Int. J. Remote Sens. 21 (9), 1911–1917. https://doi.org/10.1080/014311600209814.
Running, S.W., Thornton, P.E., Nemani, R., Glassy, J.M., 2000. Global Terrestrial Gross and Net Primary Productivity from the Earth Observing System, Methods in Ecosystem Science. Springer, New York, New York, pp. 44–57.
Saberali, S.F., Shirmohamadi-Aliakbarkhani, Z., 2020. Quantifying seed germination response of melon (Cucumis melo L.) to temperature and water potential: thermal time, hydrotime and hydrothermal time models. South Afr. J. Botany 130, 240–249. https://doi.org/10.1016/j.sajb.2019.12.024.
Stahl, K., Moore, R.D., Floyer, J.A., Asplin, M.G., McKendry, I.G., 2006. Comparison of approaches for spatial interpolation of daily air temperature in a large region with complex topography and highly variable station density. Agric. For. Meteorol. 139 (3–4), 224–236. https://doi.org/10.1016/j.agrformet.2006.07.004.
Standardization Administration of the People's Republic of China, 2008. Wheat. China Standards Press, Beijing.
Standardization Administration of the People's Republic of China, 2018. Maize. China Standards Press, Beijing.
Steduto, P., et al., 2008. AquaCrop: a new model for crop prediction under water deficit conditions. In: International Conference 'Drought management: Scientific and technological innovations. Zaragoza, Spain.
Tedeschi, A., Lavini, A., Riccardi, M., Pulvento, C., d'Andria, R., 2011. Melon crops (Cucumis melo L., cv. Tendral) grown in a mediterranean environment under saline-sodic conditions: part I. Yield and quality. Agricultural Water Manag. 98 (9), 1329–1338. https://doi.org/10.1016/j.agwat.2011.04.007.
Tedeschi, A., et al., 2017. Effect of salinity on growth parameters, soil water potential and ion composition in cucumis melo cv. Huanghemi in North-Western China. J. Agron. Crop Sci. 203 (1), 41–55. https://doi.org/10.1111/jac.12161.
Teixeira, A.H.D., Scherer-Warren, M., Hernandez, F.B.T., Andrade, R.G., Leivas, J.F., 2013. Large-scale water productivity assessments with MODIS images in a changing semi-arid environment: a Brazilian case study. Remote Sens. 5 (11), 5783–5804. https://doi.org/10.3390/rs5115783.
UNDESA, 2017. World Population Prospects: The 2017 Revision, Key Findings and Advance Tables. United Nations, Department of Economic and Social Affairs, Population Division. UN Headquarters, New York.
Van Hools, R., Eerens, H., 2015. Gio Global Land Component - Lot I "Operation of the Global Land Component", Algorithm Theorethical Basis Document - Dry Matter Productivity (DMP). In: VITO (Editor). Emergent Computation MIT Press.
Verhoef, W., 1996. Application of Harmonic Analysis of NDVI Time Series (HANTS). DLO Winand Staring Centre, Wageningen.
Veroustraete, F., Sabbe, H., Eerens, H., 2002. Estimation of carbon mass fluxes over Europe using the C-Fix model and Euroflux data. Remote Sens. Environ. 83 (3), 376–399. https://doi.org/10.1016/S0034-4257(02)00043-3.
Wang, H.Q. et al., 2012. Hydro-climatic trends in the last 50 years in the lower reach of the Shiyang River Basin, NW China. Catena, 95: 33–41.doi:10.1016/j.catena.2012.03.003.
Wart, J.V., Kersebaum, K.C., Peng, S., Milner, M., Cassman, K.G., 2013. Estimating crop yield potential at regional to national scales. Field Crops Res. 143 (1), 34–43. https://doi.org/10.1016/j.fcr.2012.11.018.
Xue, X., Liao, J., Hsing, Y.T., Huang, C.H., Liu, F.M., 2015. Policies, land use, and water resource management in an arid oasis ecosystem. Environ. Manag. 55 (5), 1036–1051. https://doi.org/10.1007/s00267-015-0451-y.
Yi, Z.W., Jia, L., Chen, Q.T., 2020. Crop classification using multi-temporal Sentinel-2 data in the Shiyang river basin of China. Remote Sens. 12 (24), 4052. https://doi.org/10.3390/rs12244052.
Zaussinger, F., et al., 2019. Estimating irrigation water use over the contiguous United States by combining satellite and reanalysis soil moisture data. Hydrol. Earth Syst. *Sc* 23 (2), 897–923. https://doi.org/10.5194/hess-23-897-2019.
Zhang, Y.L., et al., 2016. Development of a coupled carbon and water model for estimating global gross primary productivity and evapotranspiration based on eddy flux and remote sensing data. Agric. For. Meteorol. 223, 116–131. https://doi.org/10.1016/j.agrformet.2016.04.003.
Zhao, M.S., Heinsch, F.A., Nemani, R.R., Running, S.W., 2005. Improvements of the MODIS terrestrial gross and net primary production global data set. Remote Sens. Environ. 95 (2), 164–176. https://doi.org/10.1016/j.rse.2004.12.011.
Zheng, C.L., Jia, L., Hu, G.C., 2022. Global land surface evapotranspiration monitoring by a multi-process parameterization model and multi-source satellite earth observations. J. Hydrol. (Amst), 128444. https://doi.org/10.1016/j.jhydrol.2022.128444.
Zhou, J., Jia, L., Menenti, M., Gorte, B., 2016. On the performance of remote sensing time series reconstruction methods – A spatial comparison. Remote Sens. Environ. 187, 367–384. https://doi.org/10.1016/j.rse.2016.10.025.
Zhou, J., Jia, Li, Menenti, M., Liu, X., 2021. Optimal estimate of global biome – specific parameter settings to reconstruct NDVI time series with the Harmonic ANalysis of Time Series (HANTS) method. Remote Sens. 13 (21), 4251. https://doi.org/10.3390/rs13214251.
Zwart, S.J., Bastiaanssen, W.G.M., de Fraiture, C., Molden, D.J., 2010. A global benchmark map of water productivity for rainfed and irrigated wheat. Agricultural Water Manag. 97 (10), 1617–1627. https://doi.org/10.1016/j.agwat.2010.05.018.